3D printing of bending-dominated soft lattices: numerical and experimental assessment

Serena Graziosi and Federico Maria Ballo
Department of Mechanical Engineering, Politecnico di Milano, Milan, Italy
Flavia Libonati
Department of Mechanical, Energy, Management and Transportation Engineering, University of Genoa, Genoa, Italy, and
Sofia Senna
School of Industrial and Information Engineering, Politecnico di Milano, Milan, Italy

Abstract

Purpose – This study aims to investigate the behaviour of soft lattices, i.e. lattices capable of reaching large deformations, and the influence of the printing process on it. The authors focused on two cell topologies, the body-centred cubic (BCC) and the Kelvin, characterized by a bending-dominated behaviour relevant to the design of energy-absorbing applications.

Design/methodology/approach – The authors analysed the experimental and numerical behaviour of multiple BCC and Kelvin structures. The authors designed homogenous and graded arrays of different dimensions. The authors compared their technical feasibility with two three-dimensional-printed technologies, such as the fused filament fabrication and the selective laser sintering, choosing thermoplastic polyurethane as the base material.

Findings – The results demonstrate that multiple design aspects determine how the printing process influences the behaviour of soft lattices. Besides, a graded distribution of the material could contribute to fine-tuning this behaviour and mitigating the influence of the printing process.

Practical implications – Despite being less explored than their rigid counterpart, soft lattices are now becoming of great interest, especially when lightweight, wearable and customizable solutions are needed. This study contributes to filling this gap.

Originality/value – Only a few studies analyse design and printing issues of soft lattices due to the intrinsic complexity of printing flexible materials.

Keywords Cellular structures, Soft lattices, Thermoplastic polyurethane, Fused filament fabrication, Selective laser sintering

Paper type Research paper

1. Introduction

Bending-dominated lattices (Ashby, 2006) are compliant structures (Habib *et al.*, 2018). Beam-based bending-dominated cells, when compressed, undergo bending deformations rather than compression and tension (Ashby, 2006; Fleck *et al.*, 2010). Their behaviour is linear elastic until the yield point. A plateau of plastic deformation follows it until the structure becomes fully flattened, and the densification phase occurs. The stress values immediately start to rise at almost no deformation (Ashby, 2006; Bauer *et al.*, 2017). This nearly flat and long plateau, if designed to be under a safety threshold (Habib *et al.*, 2019; Mueller *et al.*, 2019), makes this type of lattices suitable for energy-absorbing applications and capable of performing better than foams (Clough *et al.*, 2019), which are nowadays the gold standard in this field (Andena *et al.*, 2019; Ashby, 2006; Habib *et al.*, 2018). Bending-dominated lattices combined with elastomeric materials represent the best solution for designing wearable, conformal (Brennan-Craddock *et al.*, 2012), lightweight and iconic structures, as personal protective equipment. However, the stress–strain curve of elastomeric bending-dominated lattices shows a monotonic increase with large deformations (Jiang and Wang, 2016), which means that the load transferred to the body increases with the stress. As lattices are non-stochastic structures Tamburrino *et al.*, (2018), their behaviour can also be tuned to this specific design target (Bertoldi *et al.*, 2017; Mueller *et al.*, 2019). For instance, at high strain rates, they can be designed to decrease the transmitted peak stress or distribute this stress over a wide range of strains (Mueller *et al.*, 2019) by transforming kinetic energy into deformation (Habib *et al.*, 2019). Such deformation could be elastic or plastic depending on whether we are looking for a multi or single-hit application (Clough *et al.*, 2019). The

The current issue and full text archive of this journal is available on Emerald Insight at: **https://www.emerald.com/insight/1355-2546.htm**

Rapid Prototyping Journal
28/11 (2022) 51–64
Emerald Publishing Limited [ISSN 1355-2546]
[DOI 10.1108/RPJ-03-2022-0095]

The authors acknowledge support from the Department of Mechanical Engineering of Politecnico di Milano under the MuSyD (Multifunctional Systems Design) project (Young Researchers Grant).

Received 25 March 2022
Revised 1 June 2022
Accepted 5 July 2022

structure response is determined by the combined effect of the following design parameters: topology and shape of the unit cells, the properties of the base material, the load orientation with respect to the lattice cells and the relative density of the lattice structure (Al-Ketan *et al.*, 2018; Ashby, 2006; Bauer *et al.*, 2017).

Elastomeric materials could also be used to make stretching-dominated structures suitable for cushioning purposes (Jiang and Wang, 2016; Kaur *et al.*, 2017). If elastomers cannot be used, the relative density of the cell can be adjusted to increase the energy absorption capabilities, even in stretching-dominated lattices (Tancogne-Dejean *et al.*, 2016), by varying the strut cross-sections accordingly. In this case, the final target is to minimize the characteristic initial peak stress of such structures and ensure an extended stress plateau. One of the most studied unit cells for energy absorption purposes is the Kelvin, whose topology mimics the geometry of foams (Brennan-Craddock *et al.*, 2012; Ge *et al.*, 2018). It also has a quasi-isotropic behaviour (Mueller *et al.*, 2019), which is an important characteristic, especially when the load direction is unpredictable. However, the material used for fabricating the structure also influences its energy absorption capabilities. For example, thermoplastic polyurethane (TPU) Kelvin lattices could be classified as rubber-like energy absorbers (Ge *et al.*, 2018), which means that TPU can be used for developing multi-hit applications (Clough *et al.*, 2019; Ge *et al.*, 2018). The body-centred cubic (BCC) is also a well-known bending-dominated structure when not loaded axially (Bauer *et al.*, 2017). This cell type is widely used because it is characterized by a geometry easily printable with a wide range of additive manufacturing (AM) technologies. It is also easy to fine-tune its stiffness by adding vertical struts (al Rifaie *et al.*, 2019) or changing their relative orientations (i.e. the angles among struts) (Abdulhadi and Mian, 2019). The strong interest in energy absorption applications has inspired several studies on how three-dimensional (3D)-printed non-stochastic structures could contribute to this field (Beharic *et al.*, 2018; Chen *et al.*, 2020; Yuan *et al.*, 2019). The relevant role played by polymer- and resin-based AM technologies has also recently stimulated an emerging enthusiasm for soft lattices (Jamshidian *et al.*, 2020). Soft lattices are cellular structures characterized by large elastic deformations because printed using rubber-like materials (Jamshidian *et al.*, 2020). This type of lattice has received less attention concerning the design, the behaviour and the influence of the printing process than those fabricated with rigid polymers (Ge *et al.*, 2018) or metals. The reasons lie in the printing process of elastomers, which is intrinsically challenging due to the characteristic properties of the parent material (Herzberger *et al.*, 2019). For example, the TPU is a flexible material often used for printing soft robotic solutions (Yap *et al.*, 2020). Yet, it is less studied than other rigid polymers, as underlined in Kasmi *et al.* (2021) for extrusion-based technologies. This is a limitation considering the number of explorable applications by combining geometric complexity and energy absorption capabilities (Kasmi *et al.*, 2021).

Nowadays, it is well-known that manufacturing-induced defects, such as porosity and dimensional inaccuracies, can significantly affect the performance of lattices, in particular metal lattice ones (Echeta *et al.*, 2020; Maconachie *et al.*, 2019). Phenomena such as strut waviness and unwanted dimensional variations of the beam thickness can decrease the elastic modulus and compressive strength of such structures (Liu *et al.*, 2017; Seepersad *et al.*, 2020). The effect of the anisotropy, due to the selected building orientation, is also widely affecting the overall mechanical performance of such structures (Stanković *et al.*, 2017). On the contrary, the influence of the printing process on the compressive behaviour of compliant soft lattices has been less investigated. Thus, it represents an emerging research field to be explored (Kolken and Zadpoor, 2017; Park and Park, 2020; Weeger *et al.*, 2019). Concerning the design aspects, while buckling phenomena can be detrimental for stiff lattices, they could represent an added value for soft structures (Jamshidian *et al.*, 2020; Yang *et al.*, 2015), which are likely to be leveraged for soft robotic applications. Yet, to understand how this phenomenon could be exploited in the case of cushioning applications, more dedicated studies are needed.

This paper investigates the mechanical behaviour of soft lattices, both homogeneous and with a graded distribution of the material, and how the printing process influences such behaviour. We designed samples conceived for a wearable application in terms of dimensional constraints. Graded arrays were used to test the influence of the printing process in the case of rapid variations, and at small scales, of the model features. Besides, graded distributions of materials represented a relevant added value for lattice design, enabling the material distribution optimization within a given design space. TPU was selected as the base material.

We first adopted simplified finite element (FE) models to design multiple BCC- and Kelvin-based lattice arrays. We then 3D printed the corresponding BCC and Kelvin arrays using two of the main AM technologies capable of printing elastomeric materials (Herzberger *et al.*, 2019): the fused filament fabrication (FFF) and the selective laser sintering (SLS). Lastly, the samples are tested under uniaxial compression. The outcome of experimental and numerical analyses allows us to draw a final discussion on the effect of the printing process on the overall behaviour of elastomeric lattice structures and which design parameters can be used to fine-tune the behaviour of soft lattices.

The paper is structured as follows: Section 2 describes the selection of the unit cells, the design and 3D printing of the samples, the numerical models and the experimental tests; results obtained from numerical simulations and experiments are provided in Section 3; in Section 4, the main outcomes are highlighted and discussed; conclusions are drawn in Section 5.

2. Materials and methods

Figure 1 shows the lattices analyzed in this work: the letter indicates the topology ("K" stands for Kelvin and "B" for BCC), while the number summarizes the in-plane (*xy* plane in Figure 1) amount of unit cells (e.g. "K5" is an array of 5 × 5 × 2 Kelvin unit cells). These cells were selected for three main reasons. Firstly, despite being widely analysed in the literature, only a few studies have tried to print them using a soft material. Secondly, some studies on printing soft lattices are available, but they focus on triply periodic minimal surface (TPMS) lattices (Holmes *et al.*, 2022). These are surface-based and not beam-based topologies. Walls and beams are topological features that could influence the

Figure 1 (a) Wireframes of the modelled Kelvin and BCC arrays. (b) The result of the thickening process applied to the arrays (the example refers to the B2 array)

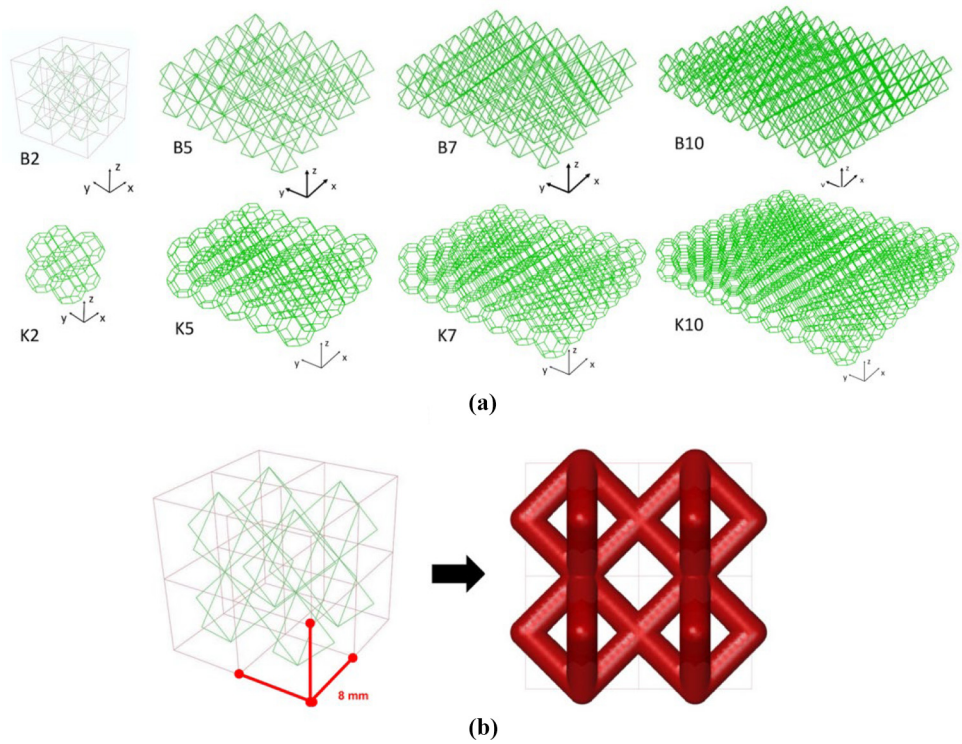

printing process differently. Thirdly, also based on the previous consideration, the two topologies were selected because they have the same theoretical behaviour (i.e. they are bending-dominated) but a significantly different number of beams and nodes (i.e. 30 beams and 24 nodes for the Kelvin and eight beams and six nodes for the BCC).

All the studied arrays have only two rows of cells in the z-direction of Figure 1. Indeed, we focused on a structure that takes up a minimal space compliant with standards in the case of a wearable hand protection pad as a potential application (ISO 21924-7:2017, 2016). We used two printing technologies to check their influence with respect to the same polymeric material, namely, FFF and SLS. FFF was selected because of its wide diffusion, and SLS was chosen because of its capability in terms of production volumes. Also, the first is an extrusion-based process, while the second is a powder-based process. Hence, they are based on different working principles.

2.1 Design of the lattice arrays

We tested multiple arrays to check the influence of both the boundary conditions and the printing process on their compressive behaviour for design spaces with different maximum dimensions. This analysis is essential, especially when scalable or customizable solutions are required. We designed arrays with the same number of voxels and comparable relative density (ρ^*) values (Table 1). Each array is built from a cubic bounding box of 8 × 8 × 8 mm (Figure 1). To design the arrays, we first set the following values of beam radius for the Kelvin:

- 0.4 mm, as the theoretical minimum printable radius of the FFF technology with a 0.4 mm diameter nozzle; and
- 0.8 mm, as a multiple of this value.

Then, the volume of the Kelvin arrays was computed, and the radii of the BCC were defined to get structures having comparable relative densities calculated as volume fractions (Table 1). These radii can be considered nominal values. To compare two different printing technologies, we intentionally started the study using nominal theoretical values to highlight later the changes to be applied to them to overcome technical

Table 1 Radii (r) and relative densities (ρ^*) of Kelvin (K) and BCC (B) arrays (Figure 1)

	K		B	
Array	r [mm]	ρ^*	r [mm]	ρ^*
2 × 2 × 2	0.4	0.07	0.55	0.06
	0.8	0.20	1.10	0.19
5 × 5 × 2	0.4	0.06	0.53	0.06
	0.8	0.21	1.05	0.20
7 × 7 × 2	0.4	0.06	0.52	0.06
	0.8	0.21	1.04	0.19
10 × 10 × 2	0.4	0.06	0.52	0.06
	0.8	0.21	1.04	0.19

issues related to the AM technology and the printability of the selected material.

2.2 Three-dimensional printing and testing of the fused filament fabrication samples

The samples were printed using the dual-extruder Ultimaker 3 machine (www.ultimaker.com), the Ultimaker TPU 95 A filament (Ultimaker, 2021) and Cura as the slicing software. The machine was equipped with a 0.4 mm diameter nozzle. The printing parameters selected to limit printing defects are summarized in Table 2 (100% infill). The option "infill travel optimisation" was enabled in the Cura profile to avoid long travelling distances, control printing time and likely reduce the oozing, a well-known problem in FFF and particularly for flexible materials, such as TPU filaments (Vassilakos *et al.*, 2021). For this filament, we considered the following properties: 0.45 (Poisson's coefficient, ν), 1.22 g/cm^3 (density, ρ), 26 MPa (Young's modulus, E) (Ultimaker, 2021).

A selection of the smallest ($2 \times 2 \times 2$) and the biggest arrays ($10 \times 10 \times 2$) was printed (Table 3) to test the influence of the printing process in two "extreme" cases and thus mimic the case in which scalable solutions are needed. The values of the printing parameters (Table 2) were not modified on purpose. The initial dimensions of the BCC arrays (Table 1) were rounded off to 1 mm (Table 3) to simplify the generation of the printing code. The BCC and Kelvin arrays with a radius lower than 0.55 mm were excluded due to the complexity of printing TPU beams with such small dimensions.

Despite the initial theoretical calculation performed to get the same relative density among the Kelvin and the BCC arrays (Table 1), the need for an effective printing process pushed us to introduce such changes. A collection of printed samples is shown in Figure 2.

2.3 Three-dimensional printing and testing of the selective laser sintering samples

SLS specimens were printed with the EOS P396 machine (www.eos.info) at an external service provider. The printing parameters were selected based on the company's experience with processing the selected material because the tuning of the SLS printing parameters was out of the scope of our study. Indeed, we wanted to show the aspects that a designer should consider when switching from one printing technology to another, keeping the same type of material. For this reason, we printed the same samples of the FFF (Table 3), but we also added arrays with a radius of 0.5/0.55 mm, to evaluate the printability of TPU beams close to the resolution limits. The printed samples are summarized in Table 4.

For the TPU powder, we considered the following properties: 0.45 (Poisson's coefficient, ν), 1.2 g/cm^3 (density, ρ), 15 MPa (Young's modulus E, retrieved experimentally). We also printed $10 \times 10 \times 2$ graded ("G") arrays designed to have the same theoretical mass and a linear density gradient: the minimum and maximum values are those of the homogenous samples, and the beam radius increases on the opposite side with respect to the applied compression load (Figure 3). These samples were printed for two main reasons. We wanted to analyse the elastic buckling effect and thus to check whether it was possible to get a controlled deformation of the structure by exploiting buckling phenomena. We also wanted to explore the influence of the printing process in the case of arrays with variable radius dimensions. An overview of the graded SLS samples and their geometry are shown in Figure 3.

Table 2 Selected printing parameters for the Ultimaker TPU 95 A filament

Printing parameter	Value
Layer height	0.15 mm
Default printing temperature	230°C
Printing temperature	230°C
Printing temperature initial layer	240°C
Build plate temperature	60°C
Retraction distance	3 mm
Retraction speed	35 mm/s

Table 3 Radii (r), relative density (ρ^*) and theoretical mass (m_t, ρ = 1.22 g/cm^3 (Ultimaker, 2021) of the FFF samples

	K (FFF)			*B* (FFF)		
Array	r [mm]	ρ^*	m_t [g]	r [mm]	ρ^*	m_t [g]
$2 \times 2 \times 2$	0.8	0.20	1.36	1.0	0.16	1.15
$10 \times 10 \times 2$	0.8	0.21	29.56	1.0	0.19	27.85

2.4 Computational modelling of the lattice arrays

Numerical simulations were carried out using Abaqus 6.14 under quasi-static linear elastic conditions. As linear elastic conditions were assumed, the validity of the numerical models presented in this paper is limited to small deformations only, i.e. results are valid only for the initial linear phase of the load–displacement curves. We selected these simplified conditions to concentrate the study on the differences between the array theoretical stiffness values and those of the as-built arrays. Considering this aim, we wanted to investigate how far is this simplified but resource-efficient model in forecasting the stiffness of the lattice. The arrays summarized in Table 1 were analysed using 3D beam and solid models. In all the models, the array was constrained by fixing the displacement of the nodes on the bottom side, while a vertical displacement was imposed at the nodes located on the upper side. A preliminary mesh convergence analysis was carried out. Different element formulations have been analysed for the beam model, namely, the Euler–Bernoulli (cubic shape functions) and the Timoshenko (with both linear and quadratic shape functions). As no significant differences were noted, the linear elements (B31 (Simulia, 2014)) were adopted for the simulations to reduce the computational effort. Starting from the curves obtained for each array, we also defined and calculated the K_0 index as:

$$K_0 = \frac{K_{array}}{n_c} \tag{1}$$

where K_{array} is the stiffness of the array, and n_c is the total number of cells of the array. K_0 represents the contribution of each cell to the stiffness of the structure. By increasing n_c, the influence of the array on the cell stiffness should decrease,

Figure 2 K2–K10 (left) and B2–B10 (right) FFF samples. Beam dimensions are available in Table 3

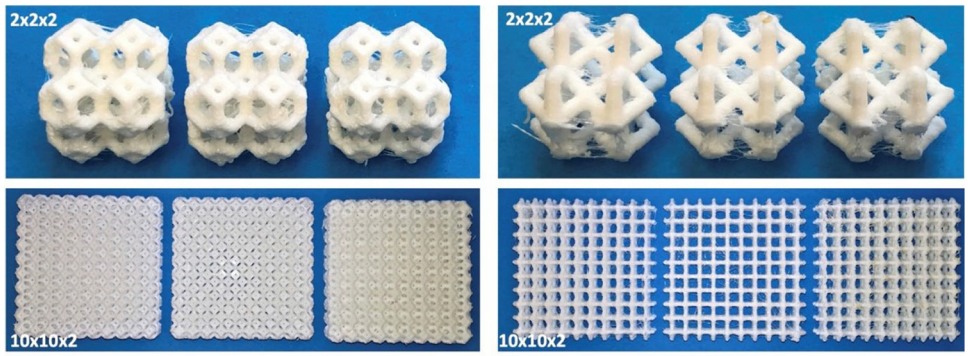

Table 4 Radii (r), relative density (ρ^*) and theoretical mass (m_t, $\rho = 1.2$ g/cm^3) of the SLS samples

Array	K (SLS)			B (SLS)		
	r [mm]	ρ^*	m_t [g]	r [mm]	ρ^*	m_t [g]
10 × 10 × 2	0.5	0.09	12.40	0.55	0.06	8.31
	0.8	0.21	29.08	1.0	0.19	27.39
10 × 10 × 2 – G	0.5÷0.8	0.13	17.64	0.55 ÷ 1.00	0.13	17.68

which means that the influence of the boundary conditions should decrease (Maskery *et al.*, 2018).

2.5 Testing of the samples

Samples were tested under quasi-static compression and displacement control. A minimum of three repetitions were verified, five in some cases. Based on the expected maximum compressive load, tests were performed on an MTS Alliance RF/150 electromechanical tensile testing machine endowed with a 150 kN load cell and on an MTS Synergy with a 1 kN load cell. A cross-head speed of 2 mm/min was adopted in the tests. Specimens were labelled specifying the printing technology and as Bn_Rh or Kn_Rh, where n is the array size (Figure 1), and Rh the struts radius (e.g. the FFF_B10_R05 is a sample having a 10 × 10 × 2 BCC array with a 0.5 mm strut radius and 3D-printed with the FFF technology).

3. Results

3.1 Effect of the array size and topology

The outcome of numerical simulations showed that BCC arrays were stiffer than Kelvin arrays. Moreover, as expected, the solid models were more rigid than the beam ones. In Figure 4, a selection of these results is provided, i.e. those obtained using the mechanical properties of the TPU filament. Being the numerical model linear elastic, the stiffness values simply scale with the array dimensions and proportionally to the material's mechanical properties.

The K_0 index value (Section 2.4) reaches a plateau over a certain number of cell repetitions (Figure 5). This means that the boundary conditions do not influence the stiffness of the array anymore. This result was already obtained in the literature for cubic samples (Libonati *et al.*, 2021; Maskery *et al.*, 2018). This type of analysis can be helpful also when analysing non-cubic design spaces, which is a situation closer to a standard design process. Figure 5 also confirms that BCC arrays are stiffer than Kelvin arrays. It is worth underlying that when scalable or customizable solutions are expected, the calculation of the K_0 index provides a valuable design

Figure 3 The 10 × 10 × 2 graded ("G") SLS samples

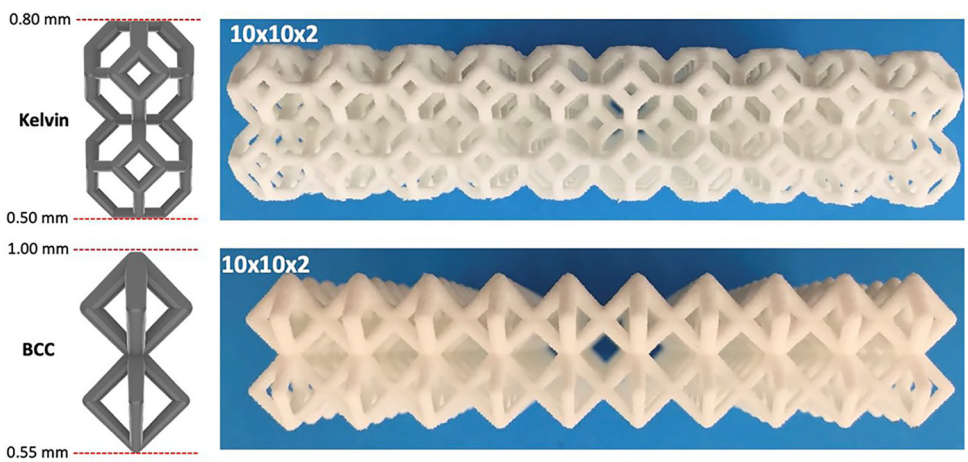

Figure 4 B5, B10, K5 and K10 beam and solid FEM results for the TPU filament arrays

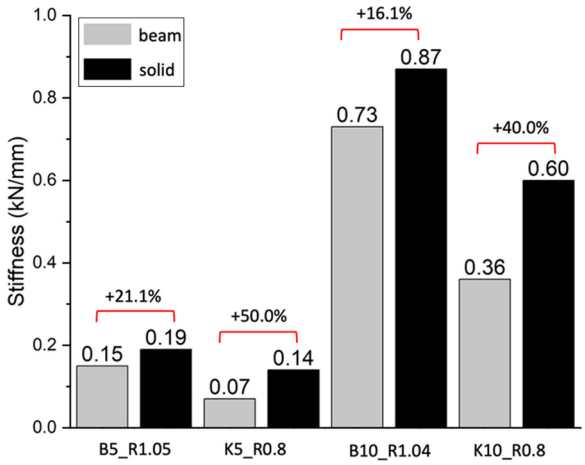

Figure 5 The K_0 index of BCC and Kelvin arrays (numerical values obtained by using the properties of the TPU filament)

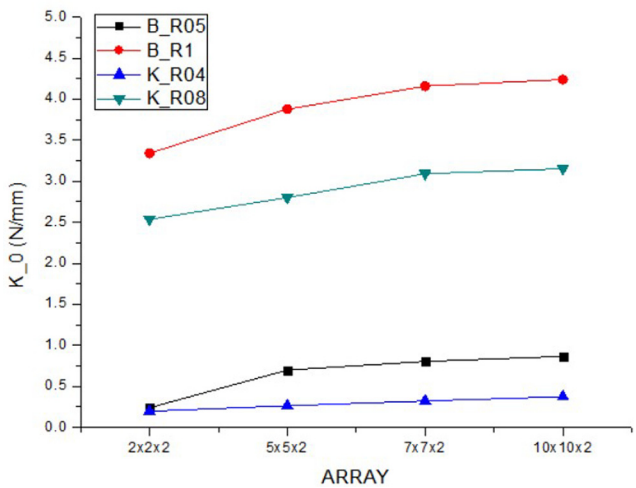

indication of how the behaviour of an array scales accordingly to its dimensions.

3.2 Effect of the printing process

The experimental and theoretical mass values of the printed samples are graphically summarized in Figure 6. The mean weight, the corresponding standard deviation (SD), the variation of the SD in percentage with respect to the mean weight are also provided. For example, for the FFF_K2 sample, these values are 1.51, ±0.1, ±6.68%, respectively. The theoretical weight for this sample is 1.36 g (i.e. FFF_K2_T).

The FFF Kelvin samples are heavier than the predicted values (Figure 6). Due to over-extrusion, these samples have a higher mass than the corresponding theoretical value, both in the case of K2 (Figure 6, top-left chart) and K10 samples (Figure 6, bottom chart). In the case of FFF BCC arrays, the over-extrusion problem is less evident than in the case of Kelvin arrays (Figure 6, top-left and bottom chart) due to the lower number of struts and the bigger values of the radius compared to Kelvin topology. It is still relevant for the B2 arrays, while in the B10 samples, we have a general under-extrusion, even if the mass values, in this case, are closer to the theoretical ones (FFF_B10 vs FFF_B10_T, Figure 6, bottom chart).

In both cases, for larger arrays, the repeatability of the process tends to decrease, as demonstrated by an increase in the standard deviation. Indeed, the standard deviations in percentage increase from 6.68 to 15.49% and from 3.17 to 5.89% for the Kelvin (K2 vs K10) and BCC (B2 vs B10) arrays, respectively (Figure 6, top-left and bottom chart). Hence, the probability of having defects is higher.

Table 5 summarizes the obtained stiffness values for the FFF samples and compares them with the numerical beam and solid model results. As also shown in Figure 7, the higher the mass value, the higher the stiffness of the array. Despite the lower mass of the BCC samples, their stiffness is comparable to that of the Kelvin samples due to the influence of the cell topology. Indeed, the BCC topology is stiffer than the Kelvin, as demonstrated by the numerical simulations (Figure 4). The over-extrusion, especially in the Kelvin samples, decreases the slenderness of the beams, and this effect reduces the likelihood of having buckling phenomena. Indeed, the load–displacement curves show a more evident monotonic increase (Figure 7), which is a characteristic of this type of elastomeric lattices (Jiang and Wang, 2016).

The SLS samples have a lower experimental mass than the theoretical values (Figure 6), but this variability is not constant. The standard deviation in percentage is quite comparable among the arrays, which demonstrates the overall good repeatability of the printing process. This aspect is even more evident in the case of Kelvin arrays, which have a higher number of struts, and in general, for bigger strut radii. The correlation between the sample stiffness and its mass was also observed for these samples (Figure 8). Besides, the fit among the measured and the simulated stiffness values for the solid model is verified when there are no significant differences among the measured and theoretical weights (SLS_K10_R08 vs SLS_K10_R08_T in Figure 6 and Table 6). The low standard deviations of the stiffness values further demonstrate the higher repeatability of the process.

The lower mass values of the SLS come with increased slenderness of the beams and thus the possibility of having unwanted buckling effects. In the load–displacement curves (Figure 8), we can observe an initial linear elastic behaviour, followed by a non-linear softening, which can be due to the micro-buckling of the struts (Jiang and Wang, 2016). This observation is valid both for the Kelvin and the BCC samples. However, in this last case, the change in slope after the linear part is abrupt and more pronounced for all the specimens due to the elastic buckling of the sloped beams, typical of BCC unit cells.

Overall, the material deficit for the SLS samples could be due to an excess of porosity, which is a known aspect for powder bed fusion processes (Ligon *et al.*, 2017). This deficit could also be due to the difficulty of printing tiny details with the TPU. Indeed, printing constraints also depend on the type of material. Overall, the influence of the mass on the stiffness is confirmed (Figure 8), as well as the fact that the BCC topology is stiffer than the Kelvin. Indeed, although the B10_R1_2

Figure 6 Mean, SD and theoretical ("T") values of the FFF and SLS samples' weight, homogeneous and graded ("G"). The value in percentage to the mean weight is also provided for the SD

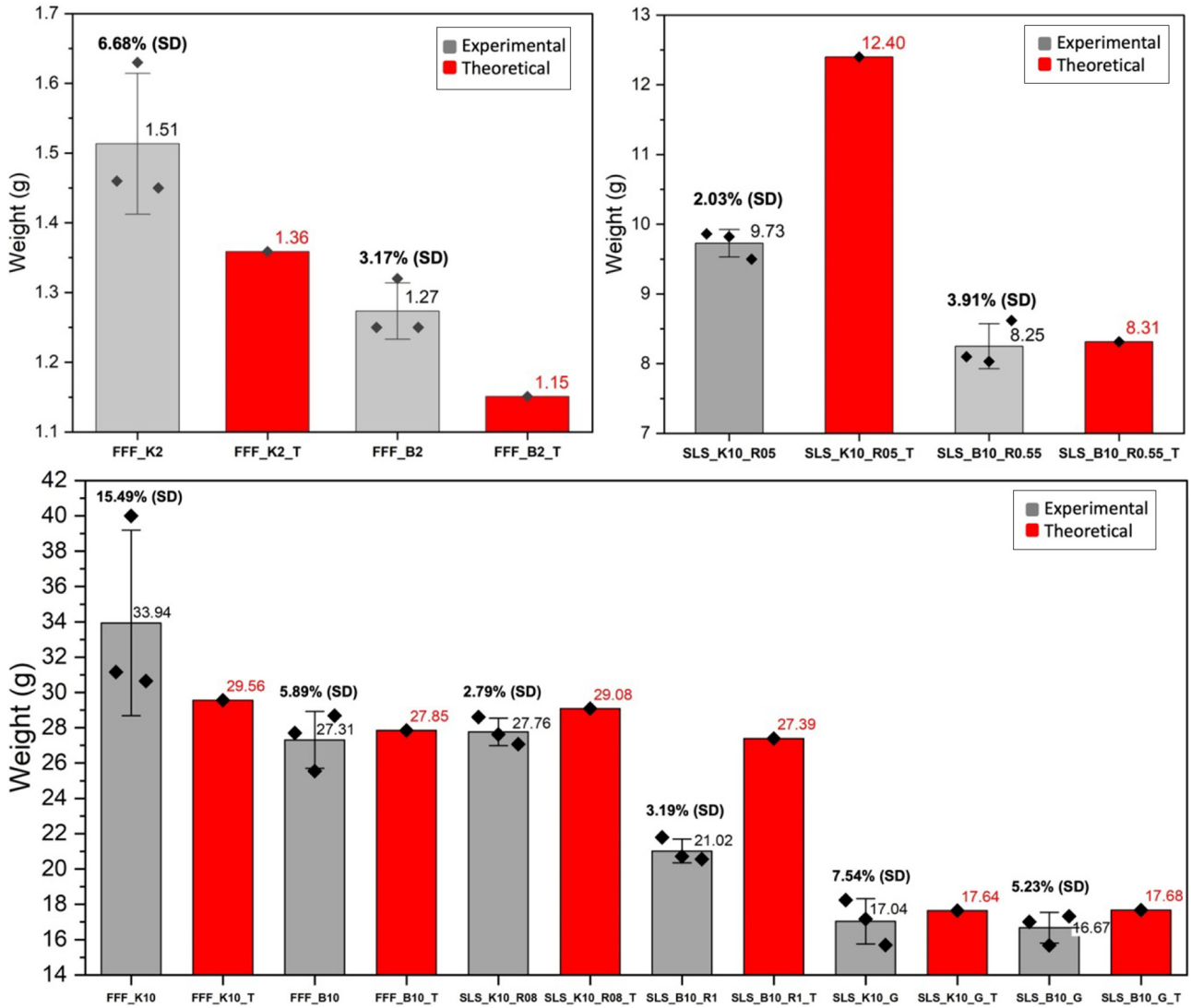

Table 5 Mean and SD of the stiffness for the FFF samples. Values are compared to the beam and solid simulations. The value in percentage to the mean stiffness is also provided for the SD

Array	Mean weight [g]	Mean stiffness [kN/mm]	SD [kN/mm]	FEM–beam stiffness [kN/mm]	FEM–solid stiffness [kN/mm]
FFF_K10_R08	33.94	1.13	0.20 (17.94%)	0.36	0.63
FFF_B10_R1	27.31	0.80	0.22 (27.91%)	0.73	0.85

sample weighs less than the K10_R08_1 sample, its stiffness is comparable (Figure 8).

3.3 Effect of the gradient

Figure 9 refers to the testing of the graded structures. These curves are mapped together with those of the homogenous samples whose radius values are used to set the gradient limits. In this case, elastic buckling is expected because it is due to the design of the beams. This effect allows the generation of a plateau once the buckling threshold is reached. In this region, the structure continues to deform with a nearly constant force until the starting of the densification phase. This design feature is essential when designing energy-absorbing applications (Seharing *et al.*, 2020; Sienkiewicz *et al.*, 2020; Wang *et al.*, 2019). This buckling is more pronounced in the BCC samples than the Kelvin ones because of the higher length-to-radius ratio of their strut. Indeed, the trend of the load–displacement curves of the BCC graded samples changes significantly compared to the homogeneous samples. This change is less evident when comparing homogenous vs graded Kelvin

Figure 7 B10 vs K10 FFF sample load–displacement experimental curves. Samples' weight and stiffness are provided in the table on the right

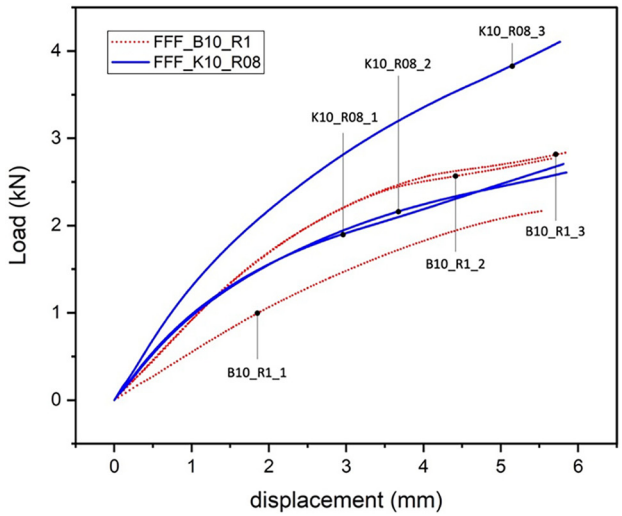

Sample	Weight [g]	Stiffness [kN/mm]
B10_R1_1	25.54	0.54
B10_R1_2	27.71	0.92
B10_R1_3	28.68	0.93
K10_R08_1	30.65	1.01
K10_R08_2	31.16	1.01
K10_R08_3	40.00	1.36

Figure 8 K10_R08 and B10_R1 SLS sample load–displacement experimental curves. Samples' weight and stiffness are provided in the table on the right

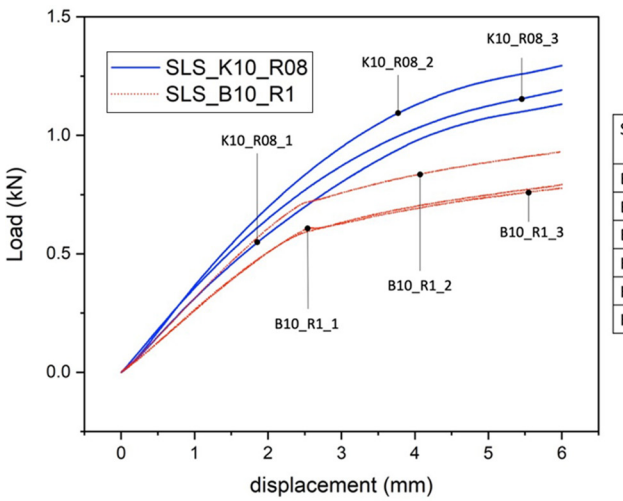

Sample	Weight [g]	Stiffness [kN/mm]
B10_R1_1	20.71	0.27
B10_R1_2	21.79	0.32
B10_R1_3	20.56	0.27
K10_R08_1	27.62	0.33
K10_R08_2	28.60	0.39
K10_R08_3	27.07	0.37

Table 6 Mean and SD of the stiffness for the SLS samples. Values are compared to the beam and solid simulations. The value in percentage to the mean stiffness is also provided for the SD

Array	Mean weight [g]	Mean stiffness [kN/mm]	SD [kN/mm]	FEM–beam stiffness [kN/mm]	FEM–solid stiffness [kN/mm]
SLS_K10_R08	27.76	0.36	0.03 (8.41%)	0.21	0.37
SLS_K10_R05	9.73	0.04	0.00	0.06	0.09
SLS_B10_R1	21.02	0.29	0.03 (10.07%)	0.39	0.51

samples. As demonstrated in Figure 6, the mass values of the graded structures are closer to the theoretical ones than in the case of homogeneous samples, even if there is a slight worsening of the process repeatability underlined by an increase of the standard deviation in percentage (Figure 6, bottom chart). However, overall, the linear change of the beam diameter increases the printability of the samples.

The experimental stiffness values (in the linear region) for the graded lattices are summarized in Table 7. Despite the lower weight of the BCC arrays, their mean stiffness is higher. We can also observe a worsening in the stiffness standard deviation compared to the homogeneous samples (Table 6) due to the slight decrease in the process repeatability (Figure 6, bottom chart).

Figure 9 Force–displacement experimental curves for graded vs homogenous arrays: Kelvin lattices (left) and BCC lattices (right)

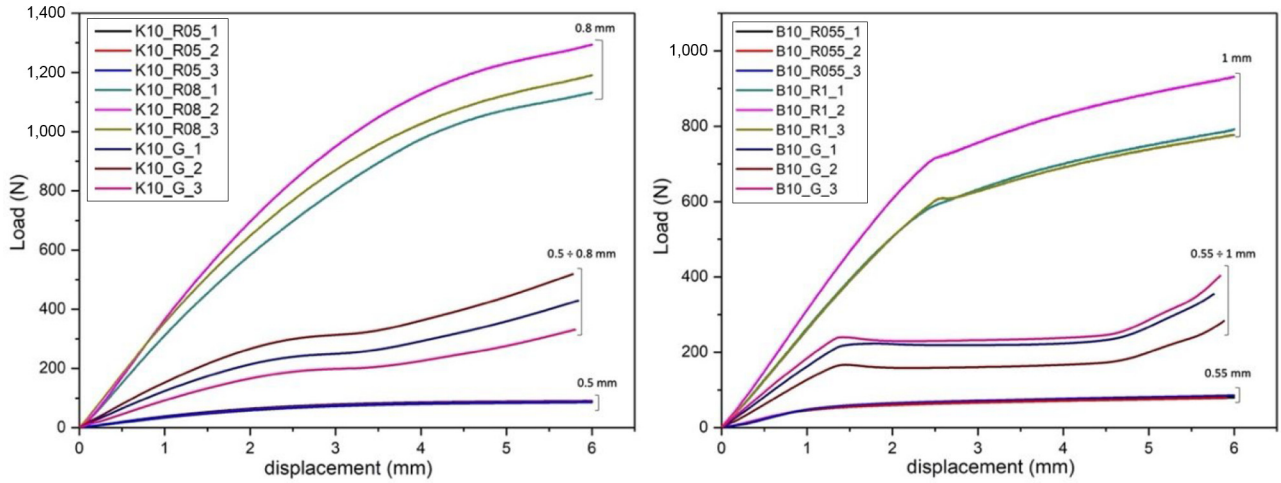

Table 7 Mean and SD of the stiffness for the SLS graded samples. The value in percentage to the mean stiffness is also provided for the SD

Array	Mean weight [g]	Mean stiffness [kN/mm]	SD [kN/mm]
SLS_K10_G	17.04	0.13	0.04 (27.73%)
SLS_B10_G	16.67	0.16	0.03 (18.70%)

3.4 Validation of the numerical models

We used the beam models to simulate B10 and K10 arrays of the SLS batch, assigning as the radius the value calculated to get a theoretical mass close to the mass of the printed samples. We called it the "Equivalent radius" (Table 8). We got an equivalent stiffness value for the BCC array that is the same as the experimental value (i.e. 0.27 kN/mm). In the case of the Kelvin array, when the strut diameter is small, the beam model correctly describes the behaviour as the same stiffness is obtained for the "Equivalent" numerical and experimental array (i.e. 0.04 kN/mm, Table 8). The fact that these two values are equal also means that the pores are randomly distributed inside the beams and not concentrated in the centre of the beam. This could have led to an increase in stiffness due to an increase in the inertia. However, when the strut diameter increases (from R5 to R8), it also increases the relevance of the nodes in influencing the behaviour of the structure (Libonati *et al.*, 2021). Hence, the equivalent stiffness (i.e. 0.20 kN/mm, Table 8) is lower than the experimental one (0.33–0.39 kN/mm, Table 8).

To derive further considerations, we calculated the relative compressive modulus, $E' = \frac{E_l}{E_S}$, of the SLS and FFF samples and of their FEM solid models (the "S" label will be used to indicate these values). E_S is the Young's modulus of the material used to 3D-print the array, and E_l is the Young's modulus of the lattice. E' is proportional to the relative density of the structure according to the following scaling law (Ashby, 2006; Bauer *et al.*, 2017):

$$E' = \frac{E_l}{E_s} \propto C\left(\frac{\rho'}{\rho_s}\right)^n \tag{2}$$

where C is a constant, and n is generally 2 for bending-dominated structures (Ashby, 2006; Bauer *et al.*, 2017). As we are considering relative values, we expect the arrays built using the same unit cell to fit in the same scaling law, independently of the printing process. Some of the obtained scaling laws are graphically represented in Figure 10, the analysis of the residuals is provided in Figure 11, while all the calculated coefficients are summarized in Table 9.

Table 8 Theoretical radius, mass and stiffness of the numerical beam-based samples reproducing the mass of the 3D-printed SLS samples

Array	Theoretical radius [mm]	Equivalent radius [mm]	Equivalent weight [g]	Equivalent FEM–beam stiffness [kN/mm]	Experimental weight–stiffness [g] – [kN/mm]
SLS_K10_R08	0.8	0.783	28.08	0.20	27.62–0.33 28.60–0.39
SLS_K10_R05	0.5	0.440	9.83	0.04	9.82–0.04 9.86–0.04
SLS_B10_R1	1.0	0.853	20.69	0.27	20.71–0.27 20.56–0.27

Figure 10 The power law of BCC (a, c) and Kelvin (b, d) samples. The "S" indicates those values obtained using the E_l of the solid FEM model of the array

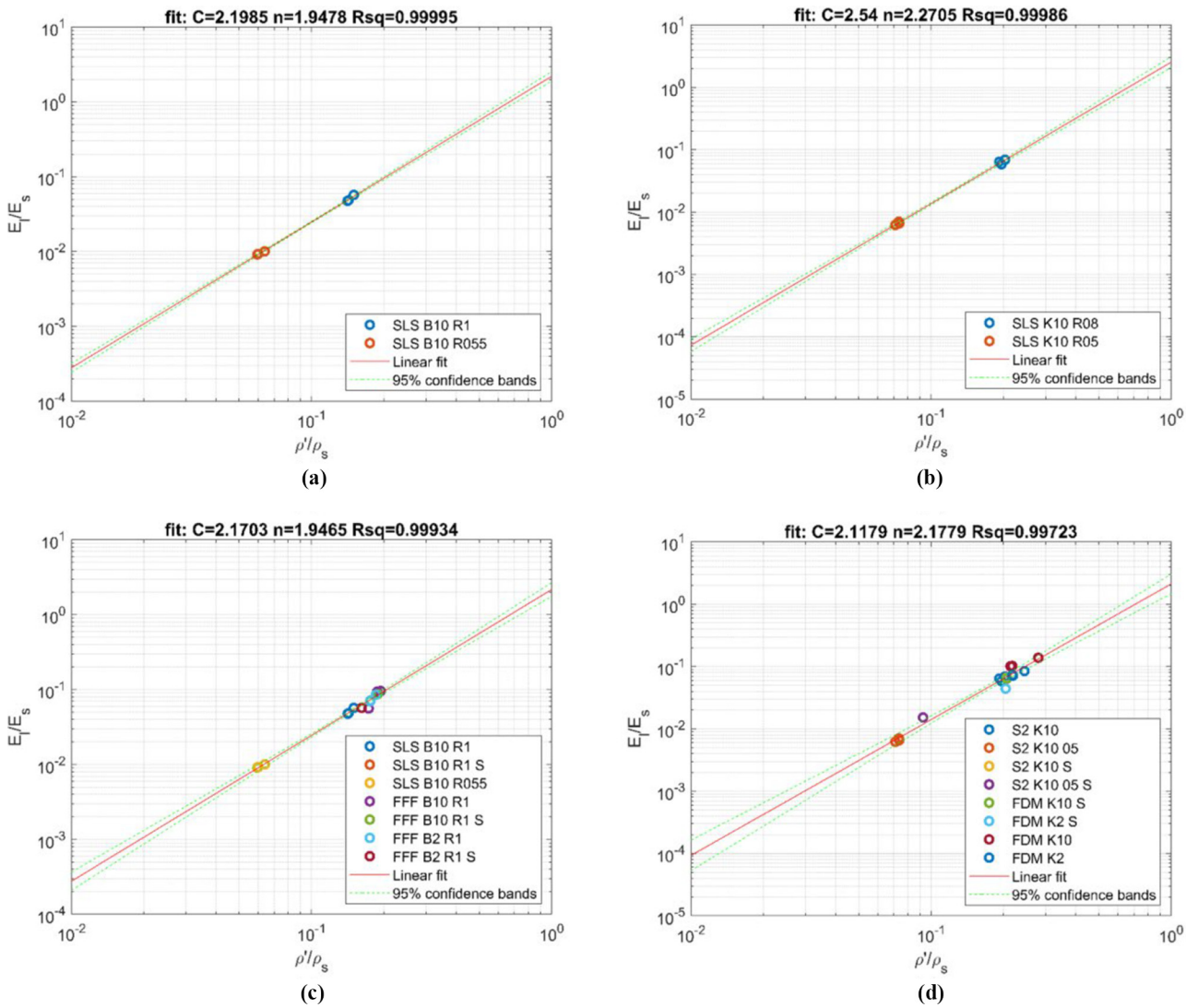

Both the BCC (Figure 10(a) and Table 9) and the Kelvin (Figure 10(b) and Table 9) SLS samples confirm their bending-dominated behaviour, despite the printing issues. The linear model adequately fits the experimental data. This consideration is confirmed by the analysis of the residuals, which follows well a normal distribution, as depicted in Figures 11(a) and 11(b), respectively. When the stiffness of the SLS solid models is also included in the fitting (i.e. R1S for the BCC and R0.8S and R0.5S for the Kelvin, Table 9 – third row), similar values of C and n are obtained for the BCC (even the n value becomes closer to 2). For the Kelvin samples, a slightly higher deviation is experienced. This fact could be confirmed by the deviation of the mass from the theoretical values, which appears to be more pronounced for the Kelvin samples (Figure 6).

If the graded structures are considered ("G", Table 9), we have the opposite situation, with a more significant change in the C and n values of the BCC than the Kelvin. Indeed, the gradient distribution of the material significantly alters the linear phase of the BCC load–displacement curves (Figure 9). When we fit all the experimental and numerical E_l values of both SLS and FFF samples, including the solid models, the obtained power laws are shown in Figure 10(c) and 10(d) for the BCC and the Kelvin, respectively. We have a more significant worsening of the linear fit for the Kelvin arrays, confirmed by the analysis of the residuals (see Figure 11(c) for the BCC and Figure 11(d) for the Kelvin). This is due to the FFF Kelvin samples, which are affected by a significant over-extrusion problem.

4. Discussion

In the case of bending-dominated structures, understanding the influence of the printing process is particularly relevant because the effective stiffness of such kind of structures scales with a factor of 2 (Ashby, 2006), which means that even a minimal loss in density can strongly affect the overall stiffness of the structure. The in-depth investigation of such influence with

Figure 11 Normal probability plots of the residuals of the linear fittings of Figures 10(a)–(d), respectively

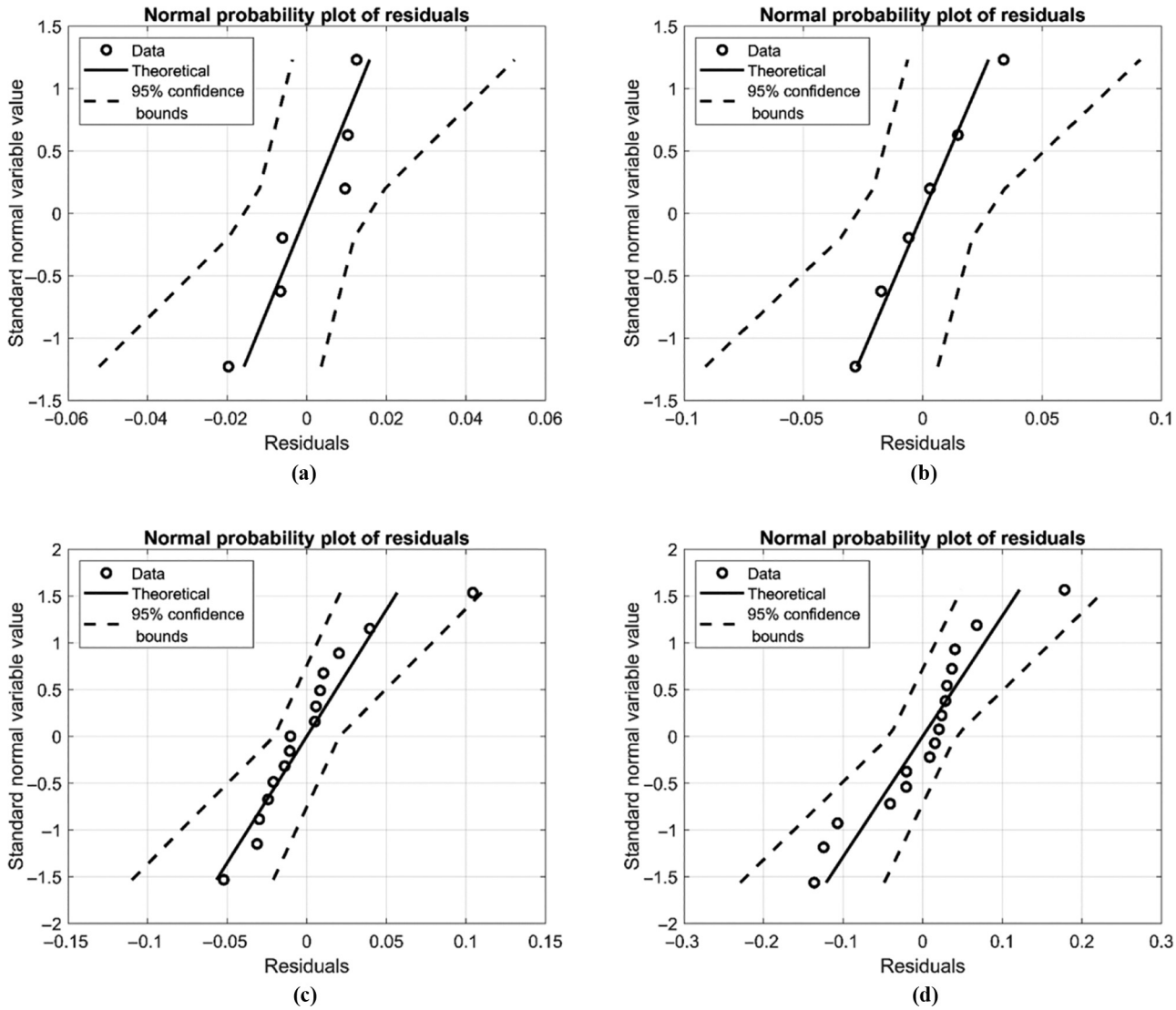

Table 9 BCC and Kelvin scaling law values (equation (2)) calculated using the relative moduli and relative densities of different combinations of arrays. "S" indicates that the sample is the FEM solid model with the specified radius (i.e. "R1S" refers to FEM solid array having a 1 mm radius), while "G" indicates the 3D-printed samples having a graded structure (Table 4)

Array	Radii [mm] of the samples	*C*	*n*	*Rsq*
SLS_B10	R1–R0.55	2.1985	1.9478	0.99995
	R1–R0.55–R1S	2.3326	1.9703	0.99993
	R1–R0.55–RG	1.7419	1.8761	0.99927
SLS_K10	R0.8–R0.5	2.5400	2.2705	0.99986
	R0.8–R0.5–R0.8S–R0.5S	2.2802	2.2059	0.99928
	R0.8–R0.5–RG	2.4801	2.2727	0.99972

respect to the selected and/or available printing process and material is thus fundamental when designing products that should exploit the potentialities of these structures. In the case of the bending-dominated soft lattices analysed in this study, the results of Section 3 can be generalized as follows.

Firstly, different influences can be noted on the sample weight (i.e. under- vs over-printing) for different cell topologies in extrusion-based processes. On the contrary, in the case of powder-based processes, the overall type of effect is almost the same (i.e. under-printing). The printing of extrusion-based TPU lattices is not straightforward because elastomeric materials can generate oozing. The increase of the filament retraction is a strategy to overcome this issue, but, in lattices, it could lead to under-extrusion defects. On the contrary, an increase in the printing temperature improves the fluidity of the melted polymer, but it could lead to over-extrusions. We had both under- and over-extrusion for the BCC arrays, while for the Kelvin, we had mainly only over-extrusion. Thus, in the case of extrusion-based processes using rubber-like filaments (e.g. TPU), if we keep the same printing parameters for the same type of cell topology, the risk is that the influence of the printing process on the final quality of the printed array can significantly vary. Hence, when printing arrays having different cell topologies but the same material, it is important to fine-tune the parameters also according to the selected cell topology.

The increased dimensions of the printed array (e.g. 2 × 2 × 2 vs 10 × 10 × 2 arrays) can lead to a more pronounced decrease in the process repeatability because it increases the likelihood of defects. Besides, arrays having strut diameters close to the resolution limit of the machine could be more challenging to be printed. When comparing the behaviour of different cell topologies at the same relative density, those having a high number of struts (i.e. the Kelvin) will inevitably have a lower strut radius. This means that, in the case of extrusion-based processes, they could be further hindered by the printing process, especially in the case of materials difficult to be processed (e.g. TPU). On the contrary, for those having a low number of struts (i.e. the BCC), the likelihood of having buckling effects is more pronounced when under-printing defects occur because the slenderness of the struts could reach a threshold value.

In the case of the SLS process, which has been demonstrated to have higher repeatability, the combination of cell radius and printing parameters appear to be the main driver of the printing process. Indeed, it is not an increase of the radius that guarantees weight values closer to the theoretical ones. We have observed contrasting behaviours among the different cell topologies (see the standard deviations in percentage provided in Figure 6). The SLS process does not suffer gravity effects like the extrusion-based process. In this case, the proper combination of the selected cell topology, radius and printing parameters determines the overall printing quality. As for the FFF, and in the case of materials difficult to be processed, it is crucial to tune the printing parameters to the array that needs to be printed.

A graded distribution of the material could represent an effective strategy to mitigate the influence of the printing process. The linear variation of the strut diameter has led to samples whose weights are closer to the theoretical ones for both cell topologies, paid by a slight decrease in the process repeatability. We could, however, tune the structure behaviour and reduce the sensitivity to the printing process through graded structures. In this case, we could also print in the same batch different types of arrays, also optimizing the printing time. The use of a graded distribution of the material appears to also be effective in providing an extended plateau in the load–displacement curves of the tested samples. The constant or nearly constant load phase is a typical and important feature of efficient energy-absorbing structures, being their response closer to those of ideal absorbers (Clough *et al.*, 2019; Fereidoon and Taheri, 2012). From an application point of view, the constant force region also allows limiting the acceleration of the body during an impact, making the graded structures analysed in this paper suitable for realizing wearable, lightweight protection devices (Clough *et al.*, 2019; Jiang and Wang, 2016). Table 10 summaries the energy absorption efficiency of the samples shown in Figure 9. These values were calculated, as suggested in Clough *et al.* (2019). In our case, we considered the area under the load–displacement curve (excluding the densification) divided by the theoretical area of the corresponding ideal absorber. This area is obtained by multiplying the peak load value of each curve by the maximum displacement of the curve.

These values provide the following insights. They confirm the efficiency gain of the BCC graded array compared to the homogeneous ones. This result is not verified in the case of the Kelvin because, as shown in Figure 9, there is not an evident flat plateau. In both cases, the Kelvin and the BCC, the arrays with the smaller radii demonstrate higher efficiency. However, in this case, the load values are low. Hence, for applications that require higher load performances, especially in the case of the BCC array, the graded structure can be more convenient.

Table 10 BCC and Kelvin samples (Figure 9) absorption efficiency

Unit cell	Radii [mm] of the samples	Absorption efficiency [%]
BCC	R0.55	75.79 ± 0.34
	R1	69.03 ± 0.38
	RG (0.55–1)	81.11 ± 0.73
KELVIN	R0.5	72.98 ± 1.28
	R0.8	64.43 ± 0.68
	RG (0.5–0.8)	64.39 ± 0.61

Concerning the numerical simulations, when the printing process plays a relevant role in influencing the quality and, therefore, the weight of the printed part, more significant discrepancies arise among numerical and experimental values. On the contrary, when there is a good fit among theoretical and real mass values, the solid model in the linear part provides a correct estimate of the structure behaviour, while the beam model tends to underestimate the stiffness of a structure. The latter effect is more pronounced in the case of cells characterized by a higher number of nodes (e.g. the Kelvin).

5. Conclusions

This study focuses on the design and 3D printing of soft lattices (i.e. lattices manufactured using elastomeric materials). They have been less explored in the literature than rigid ones thus far. Yet, they are gaining significant interest, especially when looking for a lightweight, wearable and multi-functional solution. Compared to their rigid counterparts, soft lattices are generally more challenging to be printed due to the intrinsic complexity of processing flexible materials and simulating their mechanical behaviour. To further deepen how the printing process influences the behaviour of soft lattices, we selected two bending-dominated unit cells, the BCC and the Kelvin, and we designed 3D-printed lattice pads using both the FFF and the SLS technology, using TPU as the base material. We used different printing technologies to explore how the printing process influences the performances of soft lattices. We also analysed multiple arrays whose dimensions were selected, considering the possibility of exploiting these lattices to design a wearable and scalable solution. Both homogenous and graded structures were studied. These arrays were analysed with FEM simulations in linear elastic conditions, and the numerical analyses were compared with results obtained from quasi-static compression tests. The results demonstrated that the influence of the printing process could vary according to the cell topology, diameter and array dimensions. In extrusion-based processes, the higher the number of beams and the larger the array size, the higher the probability of having printing-induced defects. In powder-based processes, the graded distribution of the material could represent an effective strategy to tune the structure's behaviour and make the structure more adaptable to the printing capability of the machine in terms of resolution.

Hence, it could represent an effective design approach to deal with the influence of the printing process, reducing the effect of the resolution-induced printing defects. This result could be in the future extended by analysing another powder-based process that allows the use of the TPU, such as the multi-jet fusion.

Lastly, numerical models, particularly solid-based models, can correctly estimate the overall structure behaviour, provided there is a good fit between theoretical and real mass values. Beam-based models, although more computationally efficient, tend to underestimate the stiffness of a structure, especially in the presence of a large number of nodes (e.g. the Kelvin), due to the intrinsic simplification of the beam formulation. Thus, they could be both used in a systematic design framework as a computational aid for soft lattice design.

References

Abdulhadi, H.S. and Mian, A. (2019), "Effect of strut length and orientation on elastic mechanical response of modified body-centered cubic lattice structures", *Proceedings of the Institution of Mechanical Engineers, Part L: Journal of Materials: Design and Applications*, Vol. 233 No. 11, pp. 2219-2233.

Al Rifaie, M., Mian, A. and Srinivasan, R. (2019), "Compression behavior of three-dimensional printed polymer lattice structures", *Proceedings of the Institution of Mechanical Engineers, Part L: Journal of Materials: Design and Applications*, Vol. 233 No. 8, pp. 1574-1584.

Al-Ketan, O., Rowshan, R. and Abu Al-Rub, R.K. (2018), "Topology-mechanical property relationship of 3D printed strut, skeletal, and sheet based periodic metallic cellular materials", *Additive Manufacturing*, Vol. 19, pp. 167-183.

Andena, L., Caimmi, F., Leonardi, L., Nacucchi, M. and de Pascalis, F. (2019), "Compression of polystyrene and polypropylene foams for energy absorption applications: a combined mechanical and microstructural study", *Journal of Cellular Plastics*, Vol. 55 No. 1, pp. 49-72.

Ashby, M.F. (2006), "The properties of foams and lattices", *Philosophical Transactions of the Royal Society A: Mathematical, Physical and Engineering Sciences*, Vol. 364 No. 1838, pp. 15-30.

Bauer, J., Meza, L.R., Schaedler, T.A., Schwaiger, R., Zheng, X. and Valdevit, L. (2017), "Nanolattices: an emerging class of mechanical metamaterials", *Advanced Materials*, Vol. 29 No. 40, p. 1701850.

Beharic, A., Rodriguez Egui, R. and Yang, L. (2018), "Drop-weight impact characteristics of additively manufactured sandwich structures with different cellular designs", *Materials & Design*, Vol. 145, pp. 122-134.

Bertoldi, K., Vitelli, V., Christensen, J. and van Hecke, M. (2017), "Flexible mechanical metamaterials", *Nature Reviews Materials*, Vol. 2 No. 11, p. 17066.

Brennan-Craddock, J., Brackett, D., Wildman, R. and Hague, R. (2012), "The design of impact absorbing structures for additive manufacture", *Journal of Physics: Conference Series*, Vol. 382, p. 12042.

Chen, X., Ji, Q., Wei, J., Tan, H., Yu, J., Zhang, P., Laude, V. and Kadic, M. (2020), "Light-weight shell-lattice metamaterials for mechanical shock absorption", *International Journal of Mechanical Sciences*, Vol. 169, p. 105288.

Clough, E.C., Plaisted, T.A., Eckel, Z.C., Cante, K., Hundley, J.M. and Schaedler, T.A. (2019), "Elastomeric micro lattice impact attenuators", *Matter*, Vol. 1 No. 6, pp. 1519-1531.

Echeta, I., Feng, X., Dutton, B., Leach, R. and Piano, S. (2020), "Review of defects in lattice structures manufactured by powder bed fusion", *The International Journal of Advanced Manufacturing Technology*, Vol. 106 Nos 5/6, pp. 2649-2668.

Fereidoon, A. and Taheri, S.A. (2012), "Using finite element method to analyze the effect of microstructure on energy absorption properties of open cell polymeric foams", *Journal of Cellular Plastics*, Vol. 48 No. 3, pp. 257-270.

Fleck, N.A., Deshpande, V.S. and Ashby, M.F. (2010), "Micro-architectured materials: past, present and future", *Proceedings of the Royal Society A: Mathematical, Physical and Engineering Sciences*, Vol. 466 No. 2121, pp. 2495-2516.

Ge, C., Priyadarshini, L., Cormier, D., Pan, L. and Tuber, J. (2018), "A preliminary study of cushion properties of a 3D printed thermoplastic polyurethane kelvin foam", *Packaging Technology and Science*, Vol. 31 No. 5, pp. 361-368.

Habib, F.N., Iovenitti, P., Masood, S.H. and Nikzad, M. (2018), "Fabrication of polymeric lattice structures for optimum energy absorption using multi jet fusion technology", *Materials & Design*, Vol. 155, pp. 86-98.

Habib, F., Iovenitti, P., Masood, S., Nikzad, M. and Ruan, D. (2019), "Design and evaluation of 3D printed polymeric cellular materials for dynamic energy absorption", *International Journal of Advanced Manufacturing Technology*, Vol. 103, pp. 2347-2361.

Herzberger, J., Sirrine, J.M., Williams, C.B. and Long, T.E. (2019), "Polymer design for 3D printing elastomers: recent advances in structure, properties, and printing", *Progress in Polymer Science*, Vol. 97, p. 101144.

Holmes, D.W., Singh, D., Lamont, R., Daley, R., Forrestal, D. P., Slattery, P., Pickering, E., Paxton, N.C., Powell, S.K. and Woodruff, M.A. (2022), "Mechanical behaviour of flexible 3D printed gyroid structures as a tuneable replacement for soft padding foam", *Additive Manufacturing*, Vol. 50, p. 102555.

ISO 21924-7:2017 (2016), "Protective equipment for martial arts Ð part 1: general requirements and test}".

Jamshidian, M., Boddeti, N., Rosen, D.W. and Weeger, O. (2020), "Multiscale modelling of soft lattice metamaterials: micromechanical nonlinear buckling analysis, experimental verification, and macroscale constitutive behaviour", *International Journal of Mechanical Sciences*, Vol. 188, p. 105956.

Jiang, Y. and Wang, Q. (2016), "Highly-stretchable 3D-architected mechanical metamaterials", *Scientific Reports*, Vol. 6 No. 1, p. 34147.

Kasmi, S., Ginoux, G., Labbé, E. and Alix, S. (2021), "Multi-physics properties of thermoplastic polyurethane at various fused filament fabrication parameters", *Rapid Prototyping Journal*, Vol. 28 No. 5, pp. 895-906, doi: 10.1108/RPJ-08-2021-0214.

Kaur, M., Yun, T.G., Han, S.M., Thomas, E.L. and Kim, W.S. (2017), "3D printed stretching-dominated micro-trusses", *Materials & Design*, Vol. 134, pp. 272-280.

Kolken, H.M.A. and Zadpoor, A.A. (2017), "Auxetic mechanical metamaterials", *RSC Advances*, Vol. 7 No. 9, pp. 5111-5129.

Libonati, F., Graziosi, S., Ballo, F., Mognato, M. and Sala, G. (2021), "3D-printed architected materials inspired by cubic bravais lattices", *ACS Biomaterials Science & Engineering*, doi: 10.1021acsbiomaterials.0c01708.

Ligon, S.C., Liska, R., Stampfl, J., Gurr, M. and Mülhaupt, R. (2017), "Polymers for 3D printing and customized additive manufacturing", *Chemical Reviews*, Vol. 117 No. 15, pp. 10212-10290.

Liu, L., Kamm, P., García-Moreno, F., Banhart, J. and Pasini, D. (2017), "Elastic and failure response of imperfect three-dimensional metallic lattices: the role of geometric defects induced by selective laser melting", *Journal of the Mechanics and Physics of Solids*, Vol. 107, pp. 160-184.

Maconachie, T., Leary, M., Lozanovski, B., Zhang, X., Qian, M., Faruque, O. and Brandt, M. (2019), "SLM lattice structures: properties, performance, applications and challenges", *Materials & Design*, Vol. 183, p. 108137.

Maskery, I., Aremu, A.O., Parry, L., Wildman, R.D., Tuck, C.J. and Ashcroft, I.A. (2018), "Effective design and simulation of surface-based lattice structures featuring volume fraction and cell type grading", *Materials & Design*, Vol. 155, pp. 220-232.

Mueller, J., Matlack, K.H., Shea, K. and Daraio, C. (2019), "Energy absorption properties of periodic and stochastic 3D lattice materials", *Advanced Theory and Simulations*, Vol. 2 No. 10, p. 1900081.

Park, J.H. and Park, K. (2020), "Compressive behavior of soft lattice structures and their application to functional compliance control", *Additive Manufacturing*, Vol. 33, p. 101148.

Seepersad, C.C., Allison, J.A., Dressler, A.D., Boyce, B.L. and Kovar, D. (2020), "Elsevier Series in Mechanics of Advanced Materials", *Uncertainty Quantification in Multiscale Materials Modeling*, Elsevier, pp. 539-565.

Seharing, A., Hadi Azman, A. and Abdullah, S. (2020), "A review on integration of lightweight gradient lattice structures in additive manufacturing parts", *Advances in Mechanical Engineering*, Vol. 12 No. 6, pp. 1-21.

Sienkiewicz, J., Płatek, P., Jiang, F., Sun, X. and Rusinek, A. (2020), "Investigations on the mechanical response of gradient lattice structures manufactured via SLM", *Metals*, Vol. 10 No. 2, pp. 1-19.

Simulia (2014), *Abaqus 6.14 Analysis User's Manual*, *Dassault Systems Simulia Corp*, Providence, RI.

Stanković, T., Mueller, J. and Shea, K. (2017), "The effect of anisotropy on the optimization of additively manufactured lattice structures", *Additive Manufacturing*, Vol. 17, pp. 67-76.

Tamburrino, F., Graziosi, S. and Bordegoni, M. (2018), "The design process of additively manufactured mesoscale lattice structures: a review", *Journal of Computing and Information Science in Engineering*, Vol. 18 No. 4, doi: 10.1115/1.4040131.

Tancogne-Dejean, T., Spierings, A.B. and Mohr, D. (2016), "Additively-manufactured metallic micro-lattice materials for high specific energy absorption under static and dynamic loading", *Acta Materialia*, Vol. 116, pp. 14-28.

Ultimaker (2021), "Technical data sheet TPU 95A", available at: https://support.ultimaker.com/hc/en-us/articles/360012664440-Ultimaker-TPU-95A-TDS (accessed 30 December 2021).

Vassilakos, A., Giannatsis, J. and Dedoussis, V. (2021), "Fabrication of parts with heterogeneous structure using material extrusion additive manufacturing", *Virtual and Physical Prototyping*, Vol. 16 No. 3, pp. 267-290.

Wang, S., Xu, Y. and Zhang, W. (2019), "Low-velocity impact response of 3D-printed lattice sandwich panels", *IOP Conference Series: Materials Science and Engineering*, Vol. 531 No. 1, p. 12056.

Weeger, O., Boddeti, N., Yeung, S.-K., Kaijima, S. and Dunn, M.L. (2019), "Digital design and nonlinear simulation for additive manufacturing of soft lattice structures", *Additive Manufacturing*, Vol. 25, pp. 39-49.

Yang, D., Mosadegh, B., Ainla, A., Lee, B., Khashai, F., Suo, Z., Bertoldi, K. and Whitesides, G.M. (2015), "Buckling of elastomeric beams enables actuation of soft machines", *Advanced Materials*, Vol. 27 No. 41, pp. 6323-6327.

Yap, Y.L., Sing, S.L. and Yeong, W.Y. (2020), "A review of 3D printing processes and materials for soft robotics", *Rapid Prototyping Journal*, Vol. 26 No. 8, pp. 1345-1361.

Yuan, S., Chua, C.K. and Zhou, K. (2019), "3D-printed mechanical metamaterials with high energy absorption", *Advanced Materials Technologies*, Vol. 4 No. 3, p. 1800419.

Corresponding author

Serena Graziosi can be contacted at: serena.graziosi@polimi.it